UCRL- 102945
PREPRINT

BUBBLE EXPANSION AND COLLAPSE NEAR A RIGID WALL

R.E. Tipton[1], D.J. Steinberg[1] and Y. Tomita[2]

[1]Lawrence Livermore National Laboratory
Livermore, CA. 94550 USA
[2]Institute of Fluid Science, Tohoku, University
Sendai, Japan

This Paper Was Prepared for Submittal to
Journal Of Fluid Mechanics

January 17, 1990

BUBBLE EXPANSION AND COLLAPSE NEAR A RIGID WALL

R.E. Tipton[1], D.J. Steinberg[1] and Y. Tomita[2]

[1]Lawrence Livermore National Laboratory, Livermore CA. 94550 USA

[2]Institute of Fluid Science, Tohoku University, Sendai, Japan

January 7, 1990

ABSTRACT

A series of experiments were performed that covered the entire range of expansion and collapse of an underwater bubble in the vicinity of a rigid wall. These experiments have been successfully simulated using a new arbitrary Lagrangian Eulerian hydrodynamic computer program which can run numerical simulations of practical bubble problems in 10 to 20 minutes of CPU time on a CRAY-YMP at an overall rate of 80 MFLOPS.

INTRODUCTION

It has been 28 years since Naudé and Ellis (1961) first observed the jet which forms inside an underwater bubble as it collapses close to a rigid surface. During the ensuing years other workers have described this collapse in more detail (Steinberg 1987), with particular attention being paid to understanding why this collapse damages the nearby surface.

In 1971, Plesset and Chapman (1971) calculated the jet formation, and in 1975, Lauterborn and Bolle (1975) showed that these calculations were in qualitative agreement with their experiments. Plesset and Chapman calculated only the bubble collapse, starting with a spherical shape and velocity field. In addition, the boundary integral method they used assumes an incompressible fluid. In 1986, Blake, Taib and Doherty (1986), also using a boundary integral method, included the expansion phase in their calculations.

We know today that the bubble, at its maximum expansion, is about 2% oblate and has a very non-spherical velocity distribution. While the water is effectively incompressible most of the time, this assumption may not be valid during the initial expansion or during the final collapse if the pressure becomes comparable to, or exceeds the bulk modulus of water (2.2 GPa). This case is true for example if the bubbles are produced by very energetic sources such as high explosives.

One of the principal discrepancies between the earlier calculations and the Lauterborn and Bolle data was that the calculated bubble remains nearly spherical during the collapse

This work was performed under the auspices of the U.S. Department of Energy by Lawrence Livermore National Laboratory under Contract No. W-7405-Eng-48.

while the data show the bubble becoming prolate quite early, reaching about 17% prolate just prior to the start of jet formation. Lauterborn (1980) has stated regarding the shape of collapsing cavities, "the conjecture is that ... jet formation depends on the curvature of the cavity-liquid interface. Parts of higher curvature collapse faster than less curved parts." Consequently, when the jet occurs depends strongly on the bubble-shape history. An additional shortcoming of the boundary integral method is that it cannot go beyond the initial formation of the jet.

The problems inherent in boundary integral methods can be overcome through the use a fast hydrodynamic computer program. The principal purpose of this paper is to show our successful numerical simulation of a complete experimental bubble expansion and collapse in the vicinity of a rigid wall.

COMPUTATIONAL DESCRIPTION

Numerical simulation of detailed bubble dynamics in two dimensions represents a technical challenge. Bubble expansion and collapse combines two extremes of hydrodynamics in one problem. During the beginning of the bubble expansion and the end of the collapse, the water and steam may be compressible, yet during the middle phase of expansion and collapse (which comprises most of the problem time) the water is effectively incompressible.

Incompressible hydrodynamics techniques exist which can handle the middle phase of the problem accurately and efficiently. However, these methods can not always be used to model the beginning or end of the problem. In principal, compressible hydrodynamics simulation programs should be able to model the entire problem. The difficulty here is that the time steps of most of these programs are restricted by the Courant stability limit and therefore may require an unacceptably large amount of computer time to run through the long middle phase of the problem. Implicit algorithms (not restricted by the Courant limit) have been used with great success in problems of one spatial dimension. In two dimensions, however, the amount of numerical work required to reach the implicit solution often exceeds the work required to reach the equivalent explicit solution, even though it must obey the restrictive Courant time step limit.

In our attempt to calculate bubble dynamics, we have found it most practical to use existing hydrodynamics algorithms for compressible fluid flow and then use several strategies to make the problems run as fast as possible. We have developed a new hydrodynamics computer program to do this. With almost every physics loop of importance vectorized, it is capable of calculating practical bubble problems in 10 to 20 minutes of CPU time on a CRAY-YMP at an overall rate of 80 MFLOPS.

Our new hydrodynamics program closely follows the algorithms of an ALE (Arbitrary Lagrangian Eulerian) hydrodynamics program developed by Barton, LeBlanc and Wilson during the 1970's (1985). For many years, this ALE program has been successfully applied

to a variety of difficult hydrodynamics problems where neither pure Lagrangian nor pure Eulerian approaches could succeed.

Lagrangian calculations are not well suited for bubble jet formation. In a pure Lagrangian calculation, the grid would distort and severely limit the time step. The Eulerian capability of an ALE program allows jet formation to be calculated without any difficulty. Using the ALE technique keeps water zones evenly spaced in radius. This keeps the time step up and still provides good numerical accuracy. It also keeps the computational grid smooth and regular in the region of the steam bubble.

The program solves the inviscid compressible hydrodynamics equations in two spatial dimensions. A computation grid (generally consisting of thousands of nodes) is used to resolve the spatial distribution of mass, momentum and energy. The hydrodynamic equations of motion are integrated by stepping through time with a discretized time step which is chosen to be small enough to guarantee numerical stability as well as reasonable accuracy. The computational cycle executed at each time step is described as follows.

First the Lagrange step is done, where all of the nodes (grid points) move as if they were embedded in the fluid. The velocities of these nodes are accelerated by pressure forces as well as by any other forces present. Then the nodes are advanced to their new locations using these new velocities. This updated grid is called the *Lagrange grid*. New volumes are calculated for the zones (or elements) bounded by the nodes and the density of each zone is updated. Finally the internal energy of each zone is updated by integrating the amount of PdV work done on it during the Lagrange step. Our Lagrange step is very similar to that found in the **HEMP** hydrodynamics program (Wilkins 1964).

Next the gridmotion step is done, where each node is tested for several types of grid distortion. If a node exceeds a preset level of distortion, then the node is "relaxed" by moving it from its Lagrangian location towards a point that lowers the grid distortions (Sharp & Barton 1981). The resulting grid is called the *generalized grid*.

Lastly the advection step is done, where the overlap volumes between the Lagrange grid and the generalized grid are calculated, and the advection of mass, momentum and energy is performed. The advection step is operator split into two sets of one dimensional sweeps. Each sweep uses a monotonic second order advection algorithm similar to the one proposed by Van Leer (1977,1979).

As mentioned earlier, we have employed several strategies designed to speed up the calculations without any effective loss in accuracy. The first of these strategies is to use polar zoning because it is naturally suited for the early and middle phases of the problem, and it requires a minimum number of nodes (around 5000) for an adequate description of the problem.

One undesirable side effect of polar zoning, however, is that it produces small zones at the center of convergence. This can produce severe Courant time step limitations. This

problem is solved by coupling groups of adjacent zones together so that they act collectively as a larger zone.

The advection step, which is relatively expensive, need not be done after each Lagrange step. Generally 5 to 10 Lagrange steps are taken for each advection step. This speeds up the calculation by a factor of 3.

Finally, during the nearly incompressible part of the problem it is not necessary to re-evaluate the water's pressure from an Equation-Of State (EOS) subroutine. Instead the much cheaper adiabatic relation can be used to update the pressure:

$$\delta p = C_s^2 \delta \rho \tag{1}$$

where δp is the change in pressure, C_s is the adiabatic sound speed and $\delta \rho$ is the change in density. The time step at which the Lagrange step runs is determined by accuracy considerations, not stability. If the time step for good accuracy is much larger than the Courant stability limit, then the Lagrange step consists of many abbreviated subcycles which use the adiabatic relation to update the pressure rather than invoke the expensive EOS subroutines. The EOS subroutines are only called at the beginning of the Lagrange step. This Courant subcycling speeds up the calculation by a factor of 2.

EXPERIMENTAL DESIGN

The experimental design has been described in detail by Shima, Takayama and Tomita (1983). Our specific experiment is shown in Fig. 1. The rigid wall is 4.2 mm below the tungsten electrodes and the water is initially at 25.1°C and 0.102 MPa. The growth and collapse of the steam bubbles, initially produced by an electric discharge across the electrodes, is recorded by a fast framing camera with an interframe time of either 5 or 10μs. To visualize the bubble interior, a back lit diffuser was used as schematically shown in fig. 2. A more complete description of the optical system can be found in Tomita & Shima (1986). In order to get complete coverage of the bubble history with such small interframe times, 12 overlapping experiments were done, each covering only a portion of the total experiment. This was accomplished by careful timing with a delay circuit.

Because the data were not all taken on one experiment, it is important to quantify the reproducibility of the system. Shima, Takayama and Tomita have carefully studied this problem. They pulsed their system numerous times with the same electrodes using a constant energy source. They found that after about the 10^{th} pulse on any given set of electrodes, the maximum bubble radius R_M remained quite constant. We have quantified these data and found that the RMS error in R_M is about 4% and the maximum error is about twice that. For the 12 experiments reported here, we found only one that differed from the average by more than 4%. Experimental error is thus about 5%.

OVERVIEW OF THE CALCULATION AND DATA

Fig. 3 shows the modified polar computational grid used at the beginning of the problem. In the angular direction, 50 equally spaced zones were used. In the radial direction, there are a total of 90 zones. Ten zones were used in the steam, and 50 equally spaced zones were used in the water between the steam-water interface and a hemispherical surface of radius 5 mm. Using a ratio of 1.05, 30 zones were used to complete the zoning out to a radius of 45 mm.

Because the size and shape of the initial steam bubble are not known, we assumed a spherical bubble of radius 0.2839 mm, which is approximately 1/10 of the maximum bubble radius. In addition, the initial energy and density are not known. We used a density of 0.1 g/cc and then chose an energy of 0.01438 J to make the maximum calculated bubble radius equal to the observed value.

The EOS for the steam bubble was a simple gamma-law gas with γ equal to 1.3. For the EOS of water we used a Grüneisen form with a non-linear shock velocity-particle velocity ($U_s - U_p$) and gamma as described by Steinberg (1987)

$$U_s = 1.48 + 2.56U_p - 1.986(\frac{U_p}{U_s})U_p + 0.2268(\frac{U_p}{U_s})^2 U_p \quad mm/\mu s, \qquad (2)$$

$$\gamma = 2.67 - 2.17/\rho \qquad 1 < \rho < \infty \qquad (3a)$$

$$\gamma = 0.5/\rho \qquad \rho < 1. \qquad (3b)$$

where the initial density is 1 g/cc.

Fig. 4 shows the computational grid at 300 μs when the bubble has reached maximum expansion. The Eulerian nature of the calculation is responsible for the smooth appearance of the grid in both the water and steam regions. The water-steam interface is still Lagrangian at this time. Fig. 5 shows the velocity vectors in the water at 300 μs. Note that the water-steam interface away from the wall has already turned around and begun to collapse, while the interface near the wall is still expanding outward. The turn-around point is located near the 4 o'clock position on fig. 5. Fig. 6 shows the calculated water-steam boundary at 605 μs. The collapsing bubble is beginning to jet, but the water-steam interface is still Lagrangian. Fig. 7 shows the computational grid and the water-steam boundary at 615 μs. The water-steam interface is now Eulerian in character. Fig. 8 shows the grid and boundary at 620 μs, just after the jet has crossed the bubble and impacted the other side.

Allowing the jet to pass through the centerpoint of the computational grid may produce two adverse effects. First, the computational time step may fall below an acceptable value. Second, the jet may suffer unphysical deformations because numerical errors tend to concentrate at the centerpoint. In our calculation both of these problems are avoided by

rezoning the bubble region at 611 μs. At that time, just before the rezoning, the water jet has pushed the centerpoint far over to the wall side of the bubble cavity, but has not yet passed through it. During the rezoning process a new computational grid is generated. This new grid is also polar in character but the centerpoint is located deep within the water jet. Only that part of the grid containing the steam bubble and the jetting water is altered. The overlap volumes between the old and new grids are calculated and the mass, momentum and energy of the old grid are transferred to the new. The calculation is then able to proceed in time. Fig. 7 shows the grid shortly after the rezone. The effect of this rezone is to pull the centerpoint through the tip of the water jet in one discontinuous jump. The calculation may then continue without any more difficulties associated with the centerpoint.

One difficulty we encountered concerned the first row of water zones next to the steam. These zones experience a radial velocity gradient throughout most of the problem. Our artificial viscosity algorithm treats this velocity gradient as if it were a shock, causing the artificial viscosity to turn on even though no shock is present. The effect of this artificial viscosity is to make the first row of water zones stiffer in the radial direction than they should be. This radial stiffness prevents the zones from compressing in the radial direction when they expand in the angular direction, and that causes the density and pressure to drop to unphysical values in those zones. This problem was solved by setting the radial velocity gradient to zero when doing the artificial viscosity calculation in the first row of water zones.

Over 90 photographs of the bubble were taken on 12 different experiments, giving good coverage of the expansion and collapse over the course of the entire problem. Rather than compare 90 photographs with 90 calculated bubble shapes, the equatorial diameter, the near pole distance, and the far pole distance were all read from the photographs as functions of time. The definitions of these terms are shown on fig. 9, and the experimental and calculated values are plotted in figs. 10-12. The 12 data sets, usually eight photographs each, are labeled A-L with each letter representing an individual photograph. The thin lines connecting the letters are merely aides for the eye. Note that at the near pole does not begin to collapse until $\sim$420μs, about 130μs after the far pole begins.

Two other useful measures are the bubble center and the prolate ratio. The former is the average of the near and far pole distances, and the latter is the ratio of the the polar diameter divided by the equatorial diameter. A prolate ratio greater than one indicates a prolate bubble; a prolate ratio less than one indicates an oblate bubble. Experimental and calculated values of these measures are shown in figs. 13 and 14.

DISCUSSION

Figs. 10-14 compare calculated and experimental measures of the bubble shape vs. time, while figs. 15 and 16 compare the complete shapes at two different times. Examination of

the time plots shown in figs. 10-14 indicate that the degree of reproducibility among the 12 experiments is good. If the initial steam energy is adjusted, it is possible to shift the calculated curve so that it agrees with the data from any single experiment. For example, a 6% increase in the initial energy will expand the maximum bubble radius by 2%, which is less than the RMS error of 4%, and shift the calculated trajectory presented in fig. 10 such that it agrees with experiments K and I.

When the bubble nearly fills the camera frame, it is difficult to measure the near and far poles relative to the optically undistorted parts of the electrodes. In some cases, the rigid wall was used as a reference, but it does not always present a sharp image on the film. Consequently, these pole distances, and hence the bubble center, have a reading error which varies among the experiments and is estimated at ±2%. Because all 12 experiments do not follow the same trajectory, the calculation presented in figs. 10-14 represents the best overall fit.

Fig. 14 shows that our calculation correctly predicts the 2% oblateness (prolate ratio of 98%) that occurs around 200 μs. The calculation also successfully predicts that the cavity shape will become prolate during the collapse of the bubble. However, we do not understand why the calculation predicts a peak prolate ratio of 1.26 whereas the data peak 20μs earlier at 1.17. Nevertheless, we find the results of this calculation encouraging. In the experiments of Lauterborn and Bolle and the earlier calculations, the distance from the wall to the initial center of the bubble was 1.5 times the maximum radius of the bubble. In our work, this ratio is 1.4, which is close enough to expect similar results when the times and distances have been scaled. In Lauterborn and Bolle, at scaled times of 72.5 and 87.5% of the way through collapse, the calculated prolate ratios of Plesset and Chapman are only about 1.05 and 1.07 respectively, those of Blake, Taib and Doherty about 1.08 and 1.11 respectively, whereas the data give values of about 1.15 and 1.18. These scaled times correspond to approximately 520 and 560 μs in our work, where our experimental and calculated values are not only in good agreement, but are similar to the experimental values of Lauterborn and Bolle.

Fig. 15 shows the calculated bubble cavity shape compared with one of the experimental photographs taken at 525 μs. Notice that the agreement in bubble size, shape and center is good. Fig. 16 shows another comparison between calculated and experimental bubble cavity shape at 605 μs. In this case, the bubble shape and center agree well, but the overall size of the calculation is smaller than the experiment. However, at this late time, even a minor problem with the numerical simulation can show up as an significant difference between it and the experiment, because the bubble system is changing so rapidly. The velocity of the jet at this time is approximately 100 m/s.

Fig. 17 presents the calculated pressure at the rigid wall as a function of time. The pressure has been spatially averaged along a disc of diameter 6 mm to approximate the pressure pulse seen by a Swiss Kistler gauge. The plot shows the pressure from both the initial bubble explosion as well as the pressure spike from the bubble collapse.

An intuitive explanation for why the collapsing bubble forms a jet can be seen by examining figs. 13 and 18. Fig. 13 shows that during the expansion phase, 0-300μs, the bubble center moves slightly away from the wall, but during the collapse phase, 300-600μs, the center of the bubble moves rapidly towards the wall. This motion towards the wall is because, as the bubble collapses, the water surrounding the bubble is forced to expand, and its pressure drops. The pressure drops more rapidly on the side of the bubble facing the wall because there is less water available to flow into the volume previously occupied by the steam bubble. It is this difference in pressure which moves the center of the bubble towards the wall. Further away from the bubble, however, the velocity field of the water is still converging upon the original center of the bubble. As a consequence, the converging flow of the water stagnates off-center late in time, forming a region of high pressure which lies just outside the bubble. This region of high pressure is easily identified in fig. 18. It is this off-center convergence of the water, and the resulting pressure peak which forms outside the bubble, that causes the jet to form.

We also examined a variety of issues concerning the validity of our calculational approach. Calculations which included the tank walls and the water-air surface inside the tank were done and showed that there was no significant effect due to them. This is a non-trivial conclusion, since sound signals have ample time to travel between the bubble and the tank wall or the water-air surface several times during the course of the experiment. The initial density of the steam bubble was varied from 1 g/cc to 10^{-3} g/cc with no significant effect observed on the bubble shape. Using the measured initial values of temperature and pressure produced no effect compared with the use of the nominal STP conditions of 300°K and 1 atmosphere.

The effects on the bubble shape due to the complexity of the EOS of the water and steam were studied and found to be minor. We found that the water EOS could be simplified from eqns. 2 and 3 and modeled equally well as a fluid with a constant bulk of 2.2 GPa. We varied this bulk modulus from 1.5 GPa to 3.0 GPa and the adiabatic exponent of the steam from 1.2 to 1.666 and observed that the calculated results were insensitive to these variations. Finally, zoning sensitivity studies were done to verify that our calculations had converged.

One of the major difficulties in simulating bubble expansion and collapse experiments is that the size, shape, density and energy of the initial steam bubble are unknown. One solution to this problem would be to use a few milligrams of high explosive (HE) as an energy source. In this way, the geometry, density and initial energy can be completely specified. Such small quantities of HE are not difficult to work with in a laboratory environment.

An additional advantage is that it is easy to produce bubbles a few tens of centimeters in diameter. At this size, the bubble is much larger than a typical pressure gauge, such as the Swiss Kistler transducer. These gauges do not have a uniform pressure response over their face (Tomita, Shima & Ohno 1984) which is a problem if the bubble is much smaller

than the gauge. With a bubble that is much larger, absolute pressure measurements can be made. Of course, in this case the effect of gravity must be taken into consideration.

An HE bubble is not a vapor bubble, but contains non-condensable HE product gases. However, this too is not a problem, as good representations of the EOS of these product gases exist. Finally, our experience has shown that eqns. 2 and 3 will be adequate to describe the EOS of water under the conditions of strong HE shocks (Steinberg 1987).

CONCLUSION

After a successful comparison to a body of experimental data, a modern hydrodynamic computer simulation program allows the user to examine other thermomechanical variables in an expanding and collapsing bubble to a degree not readily achievable experimentally. We have made such a successful comparison of bubble shape and size vs. time. The simulations now permits us to view the velocity and pressure fields as illustrated in figs. 5 and 18. In addition, numerical simulations give the user the flexibility to examine even more challenging problems, such as very non-spherical bubbles, bubble-bubble or shock-bubble interactions. We hope to make such calculations the subject of future investigations.

REFERENCES

BARTON, R.T. 1985 Development of a multimaterial two-dimensional, arbitrary Lagrangian-Eulerian mesh computer program. In *Numerical Astrophysics*, J.M. Centrella, J.M. LeBlanc, R.L. Bowers, eds., Jones and Bartlett Publishers, Inc. Boston. pp. 482-497.

BLAKE,J.R., TAIB,B.B. & Doherty,G. 1986 Transient cavities near boundaries. Part 1. rigid boundary. *J. Fluid Mech* **170**, 479-497.

LAUTERBORN,W. & BOLLE,H. 1975 Experimental investigation of cavitation- bubble collapse in the neighborhood of a solid boundary *J. Fluid Mech.* **72**, 391-399.

LAUTERBORN,W. 1980 Cavitation and coherent optics. In *Proc. 1st Intl. Conf. Cavitation and Inhomogeneities in Underwater acoustics*, Gottingen, pp. 3-12.

NAUDÉ,C.F. & ELLIS,A.T. 1961 On the mechanism of cavitation damage by nonhemispherical cavities collapsing in contact with a solid boundary. *J. Basic Engng.* **83**, 648-656.

PLESSET,M.S. & CHAPMAN,R.B. 1971 Collapse of an initially spherical vapor cavity in the neighborhood of a solid boundary *J. Fluid Mech.* **47**, 283-290.

SHARP,R.W. Jr. & BARTON,R.T. 1981 EMI ejection model. Lawrence Livermore National Laboratory, UCID 17809.

SHIMA,A., TAKAYAMA,K. & TOMITA,Y. 1983 Mechanism of impact pressure generation from spark-generated bubble collapse near a wall. *AIAA Journal* **21**, 55-59.

STEINBERG,D.J. 1987 A brief review on cavitation bubble collapse near a solid boundary. Lawrence Livermore National Laboratory, UCID-21054.

STEINBERG,D.J. 1987 Spherical explosions and the equation of state of water. Lawrence Livermore National Laboratory, UCID-20974.

TOMITA,Y., SHIMA,A. & OHNO,T. 1984 Collapse of multiple gas bubbles by a shock wave and induced impulsive pressure. *J. Appl. Phy.* **56**, 125-131.

TOMITA,Y. & SHIMA,A. 1986 Mechanisms of impulsive pressure generation and damage pit formation by bubble collapse. *J. Fluid Mech.* **169**, 535-564.

VAN LEER,B. 1977 Towards the ultimate conservative difference scheme III. Upstream-centered finite-difference schemes for ideal compressible flow. *J. Comp. Phys.* **23**, 263-275.

VAN LEER,B. 1979 Towards the ultimate conservative difference scheme V. A second-order sequel to Godunov's method. *J. Comp. Phys.* **32**, 101-136.

WILKINS,M.L. 1964 Calculations of elastic-plastic flow. In *Methods of Computational Physics*, B.J. Alder, S. Fernbach, and M. Rotenberg, eds., Academic Press, New York, vol. III, pp. 211-263.

FIGURE CAPTIONS

1. Experimental Design
2. Schematic of the optical observation system
3. Initial Computational Grid
4. Computational Grid and Bubble Shape at 300 μs
5. Velocity vectors in water at 300 μs
6. Computational Grid and Bubble Shape at 605 μs
7. Computational Grid and Bubble Shape at 615 μs
8. Computational Grid and Bubble Shape at 620 μs
9. Definition of Terms: Equatorial Diameter, Near Pole Distance and Far Pole Distance
10. Position of the Equatorial Diameter vs. Time
11. Position of the Near Pole vs. Time
12. Position of the Far Pole vs. Time. Note suppressed zero.
13. Position of the Bubble Center vs. Time. Note suppressed zero.
14. The Prolate Ratio vs. Time
15. Comparison of the Experimental and Calculated Bubble Shape at 525 μs.
16. Comparison of the Experimental and Calculated Bubble Shape at 605 μs.
17. Calculated Pressure at the Wall vs. Time
18. Isobaric Contours at 600μs

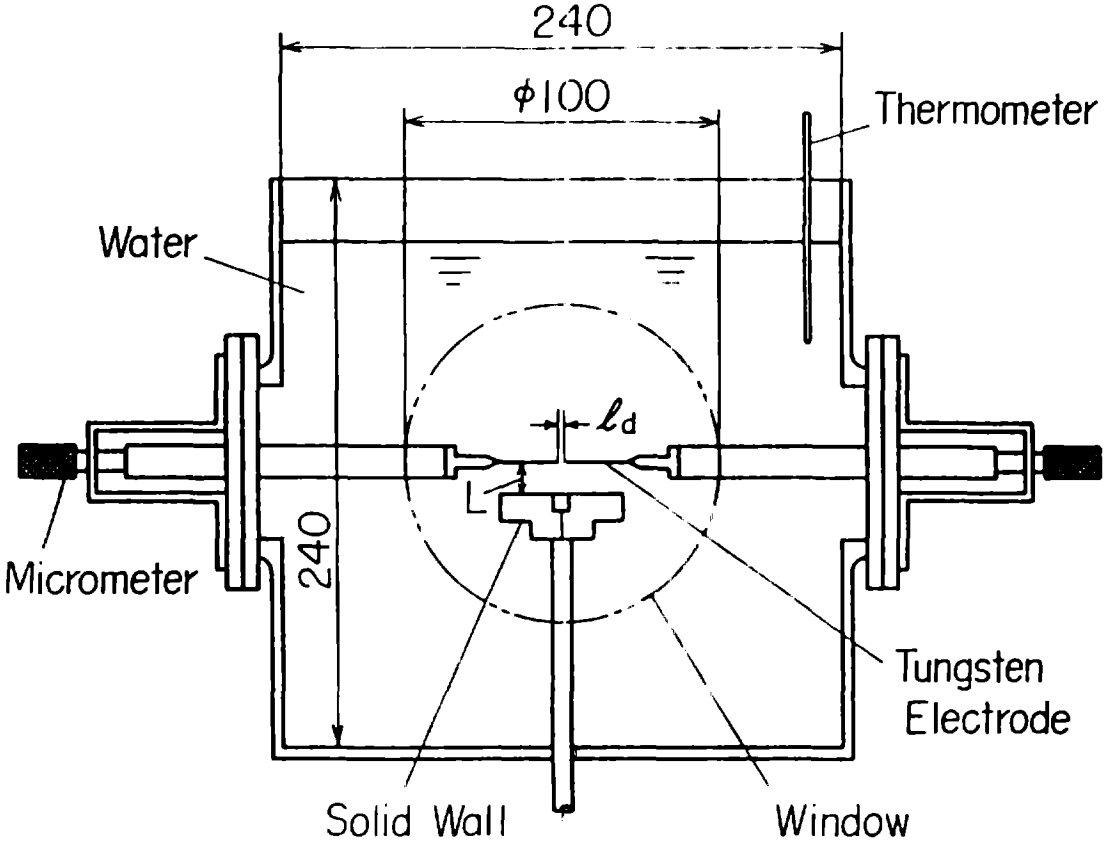

Fig. 1. Experimental Design

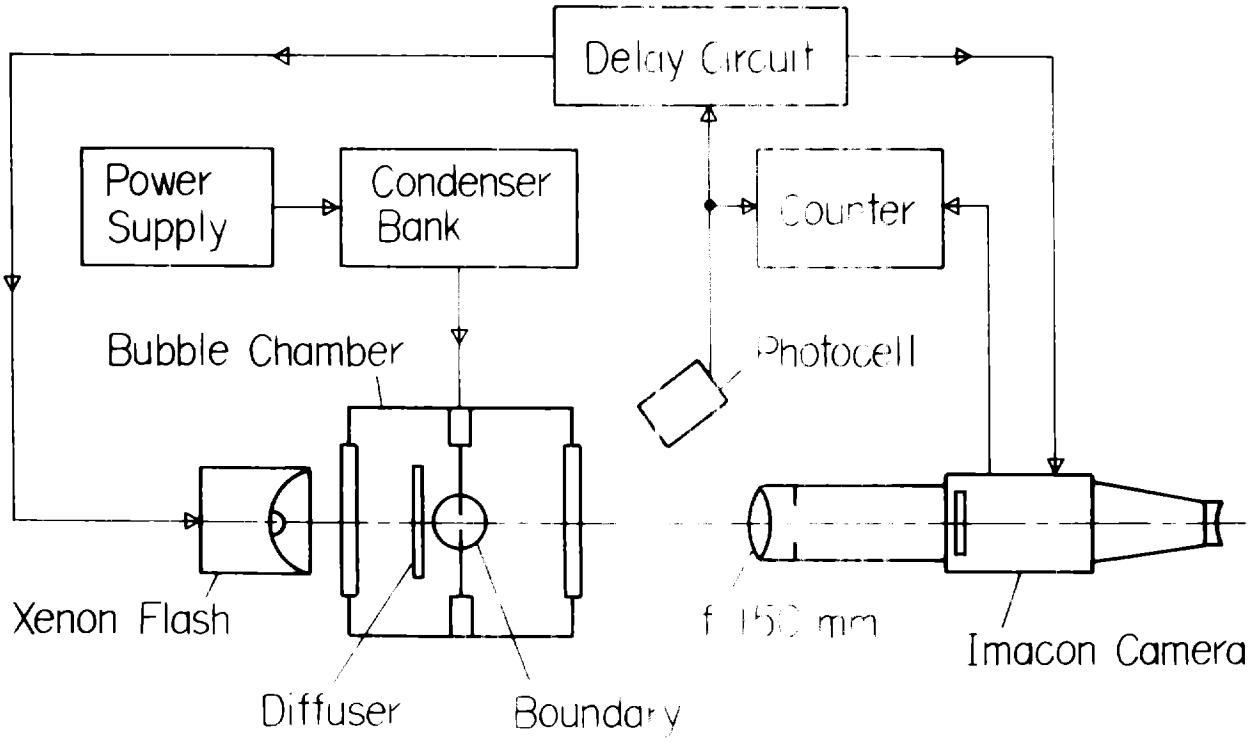

Fig. 2 Schematic of the optical observation system.

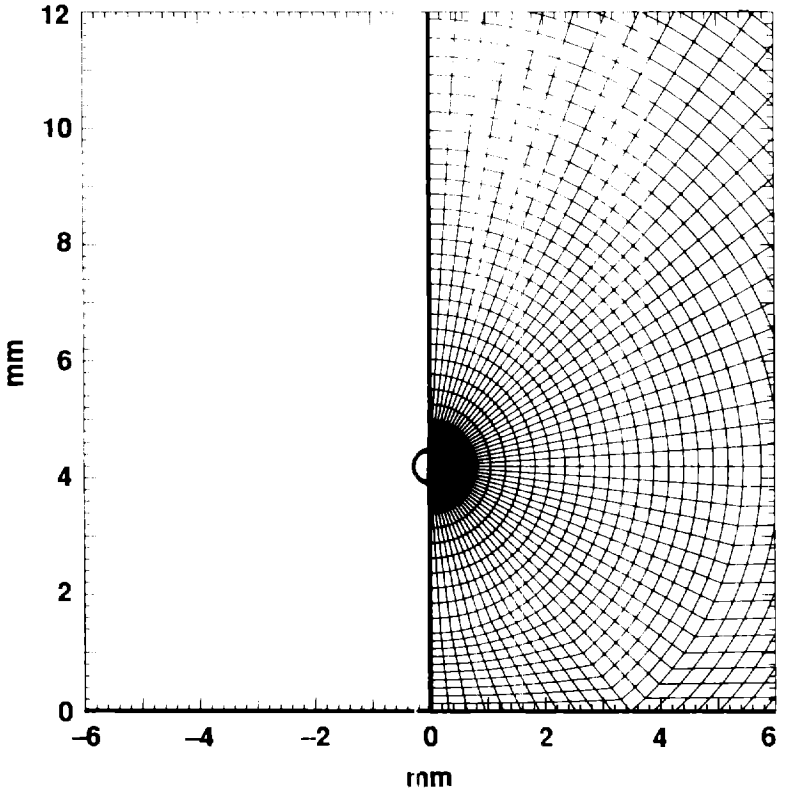

Fig. 3 Initial computational grid

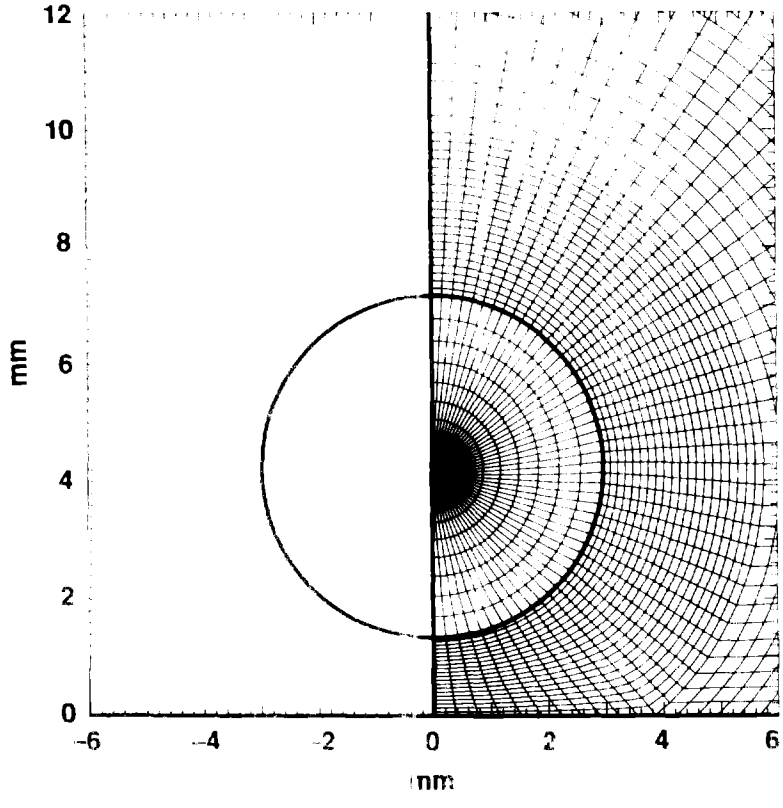

Fig. 4 Computational grid and bubble shape at 300 μs

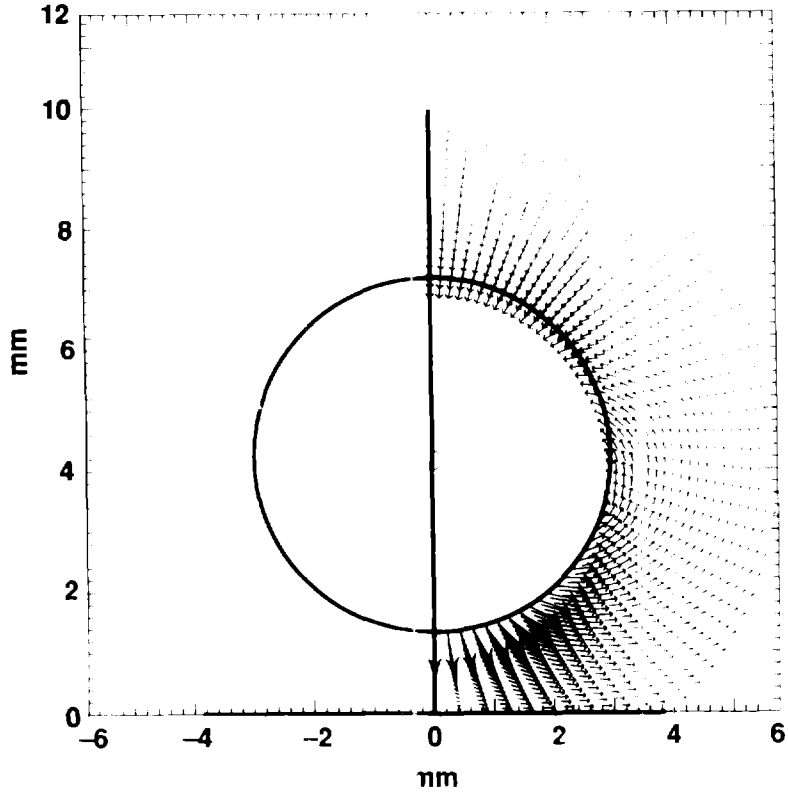

Fig. 5 Velocity vectors in water at 300 μs

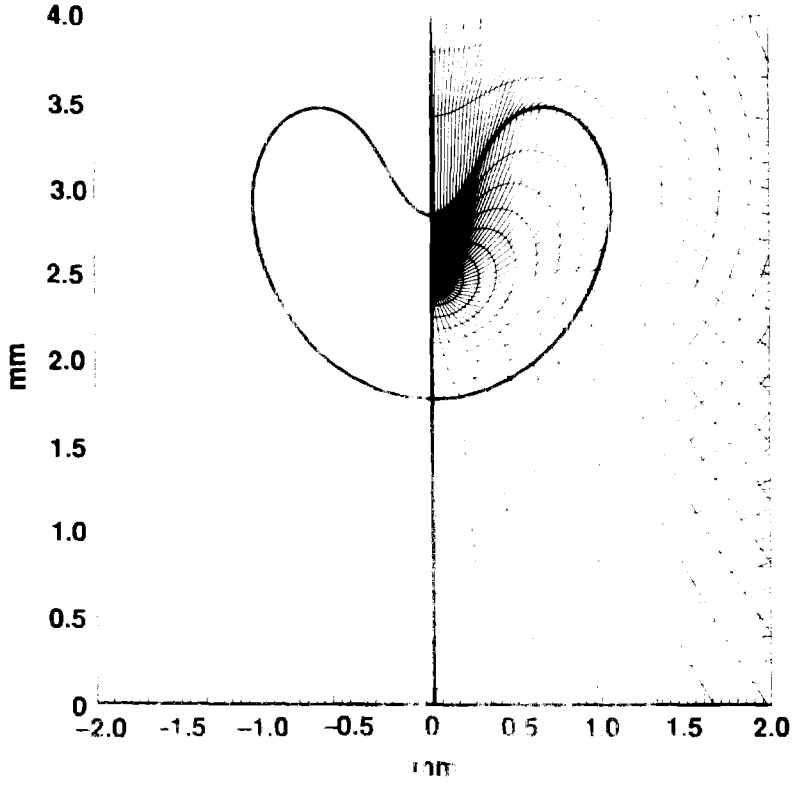

Fig. 6 Computational grid and bubble shape at 605 μs

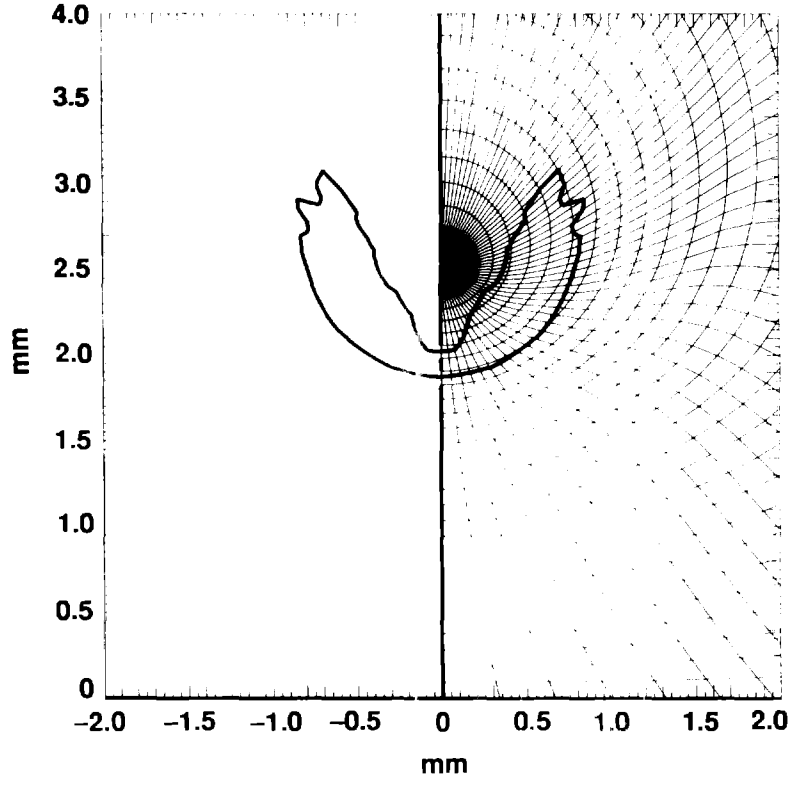

Fig. 7 Computational grid and bubble shape at 615 μs

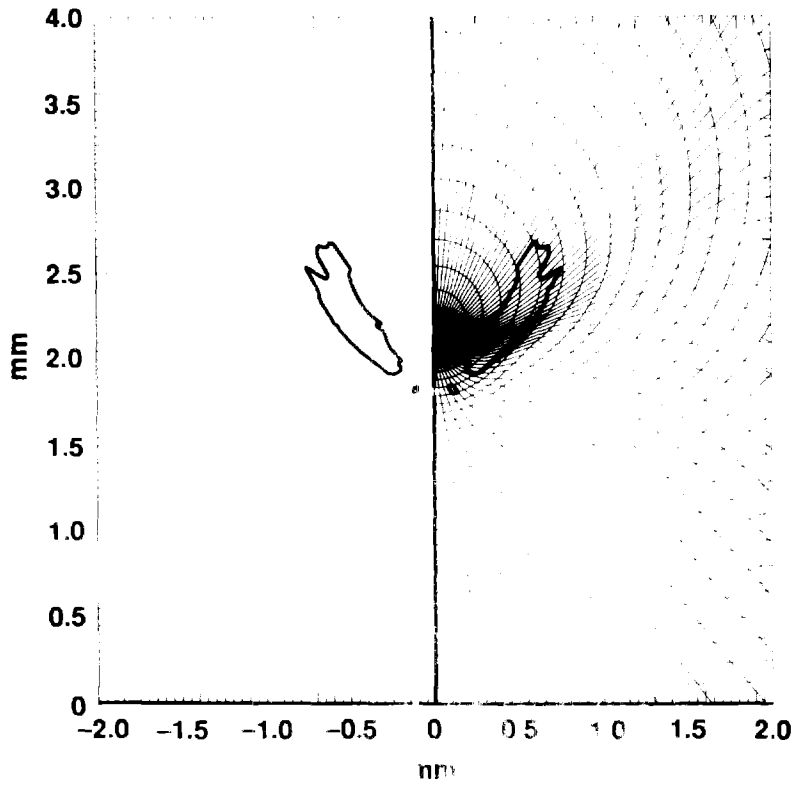

Fig. 8 Computational grid and bubble shape at 620 μs

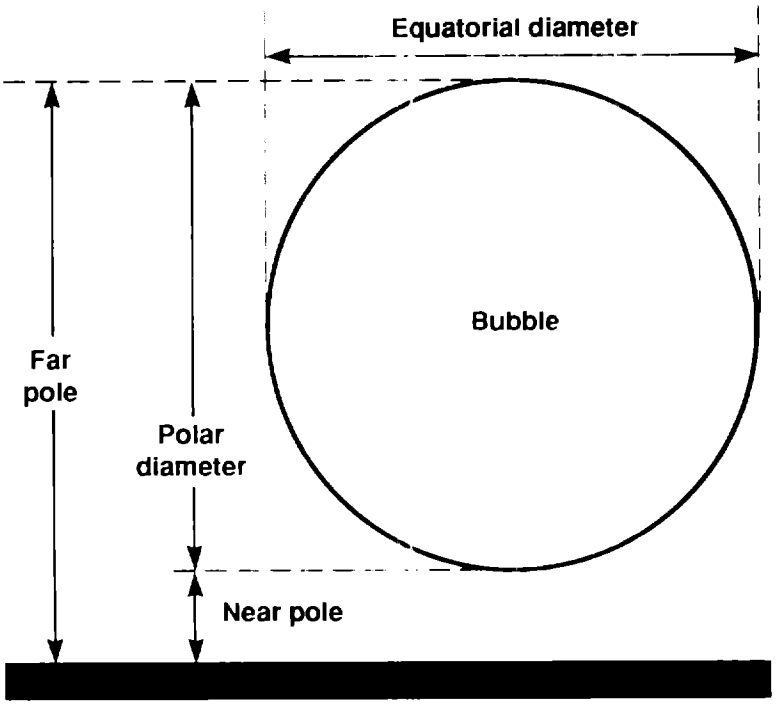

Fig. 9 Definition of terms: equatorial diameter, near pole distance and far pole distance

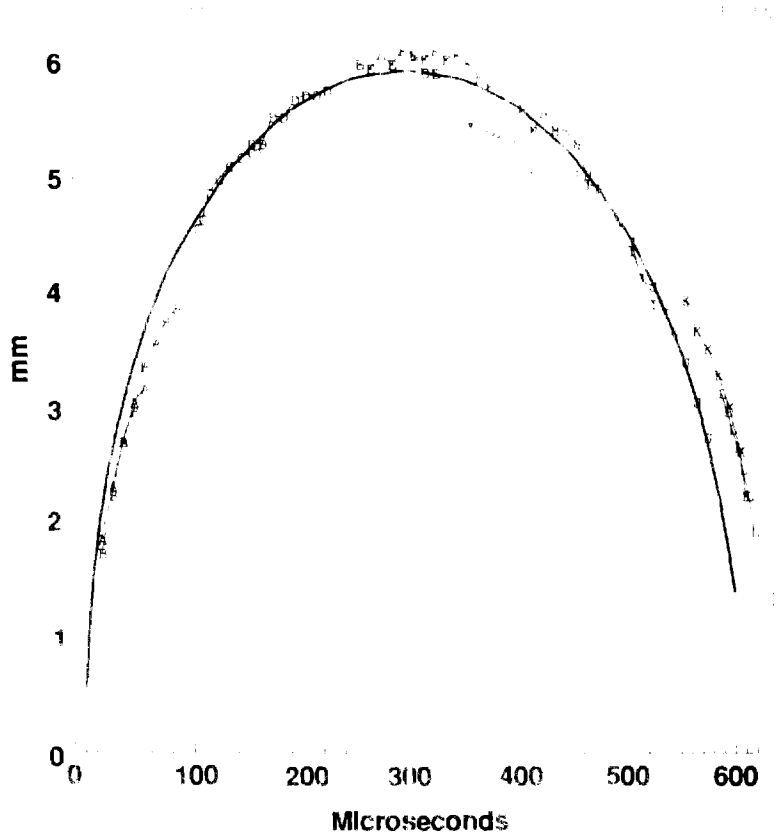

Fig. 10 Position of the equatorial diameter vs. time

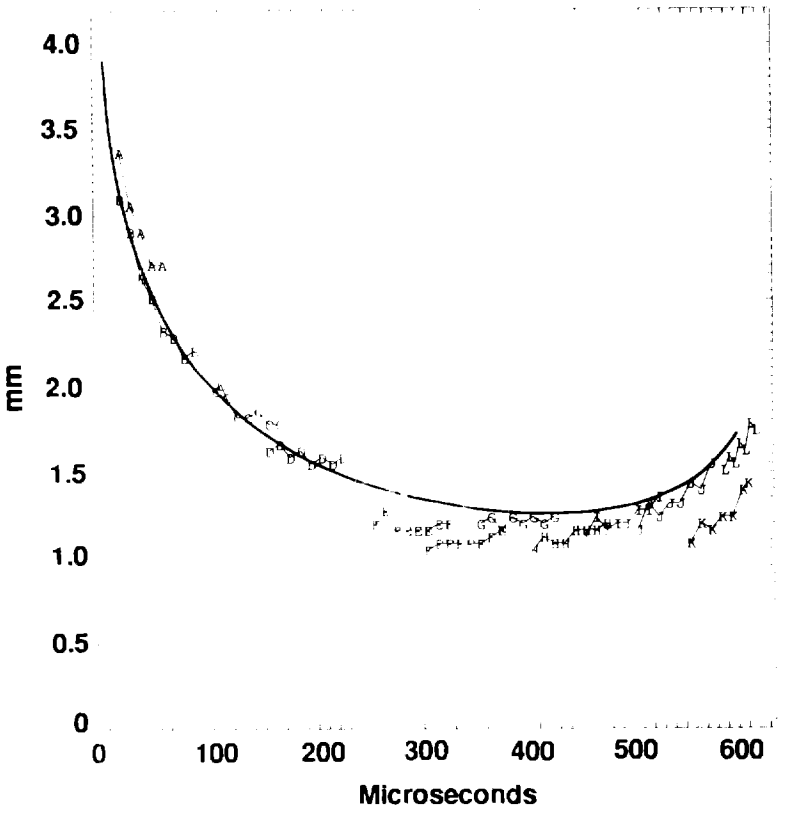

Fig. 11 Position of the near pole vs. time

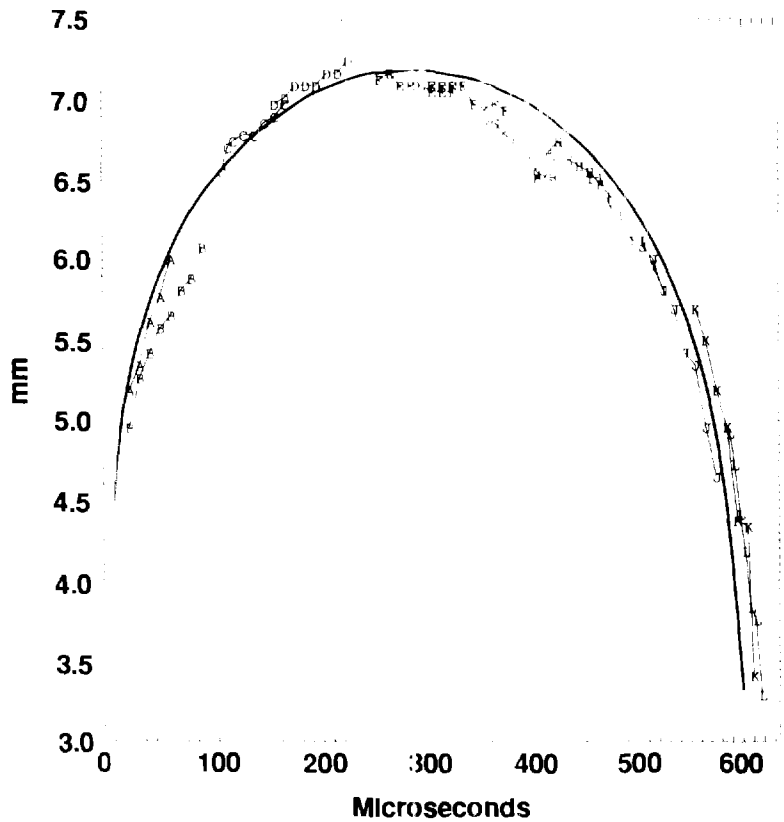

Fig. 12. Position of the far pole vs. time. Note supressed zero.

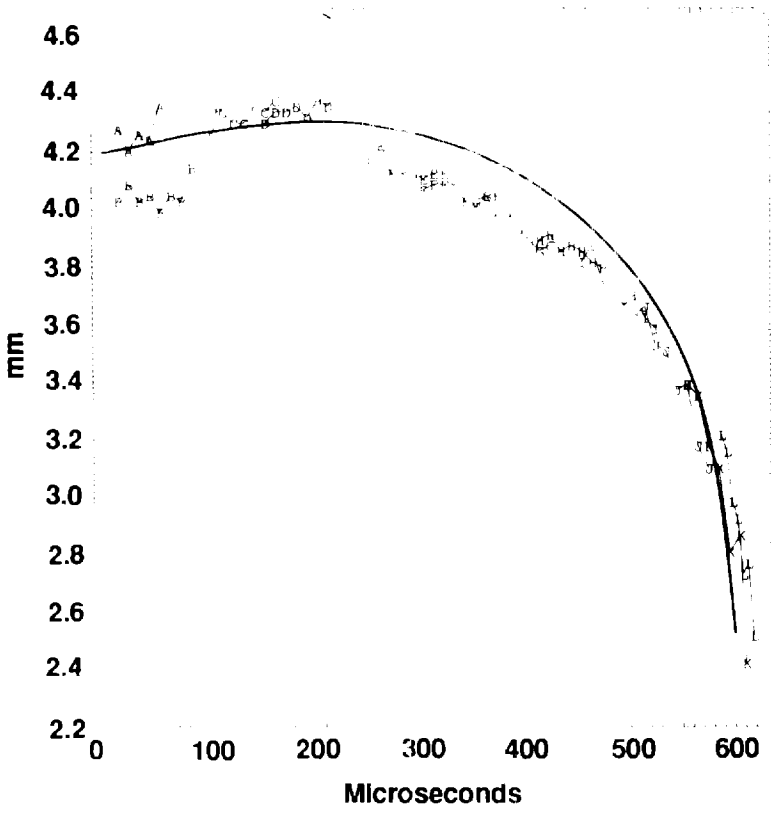

Fig. 13 Position of the bubble center vs. time.
Note supressed zero

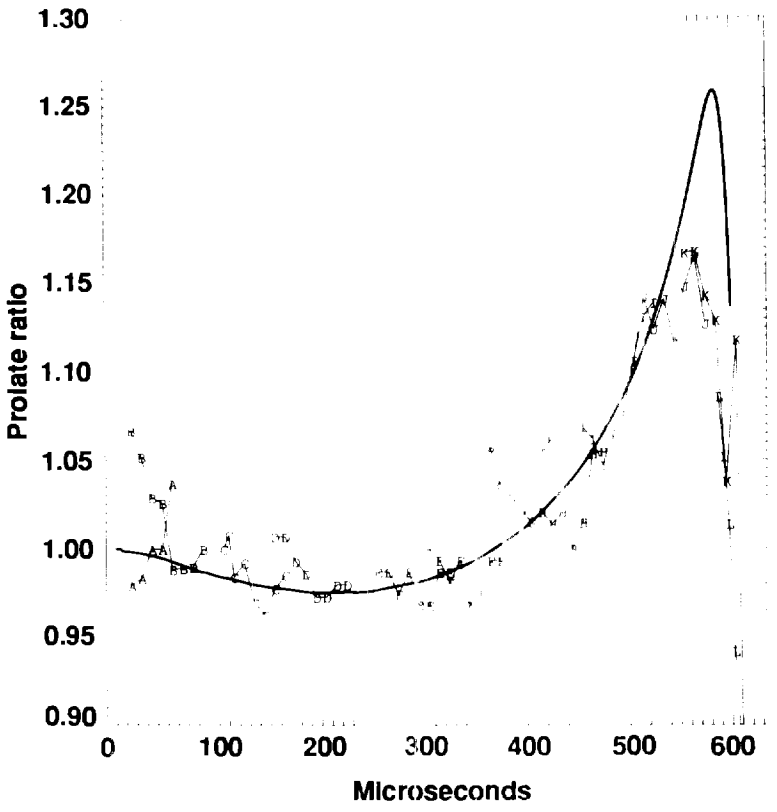

Fig. 14 The prolate ratio vs. time

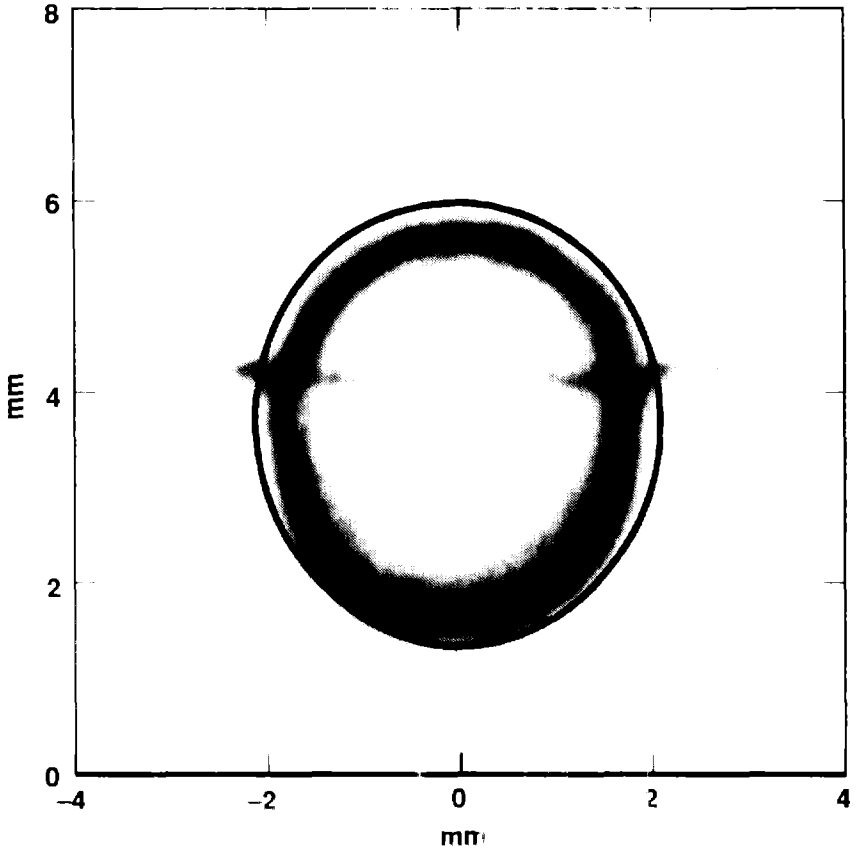

Fig. 15 Comparison of the experimental and calculated bubble shape at 525 μs

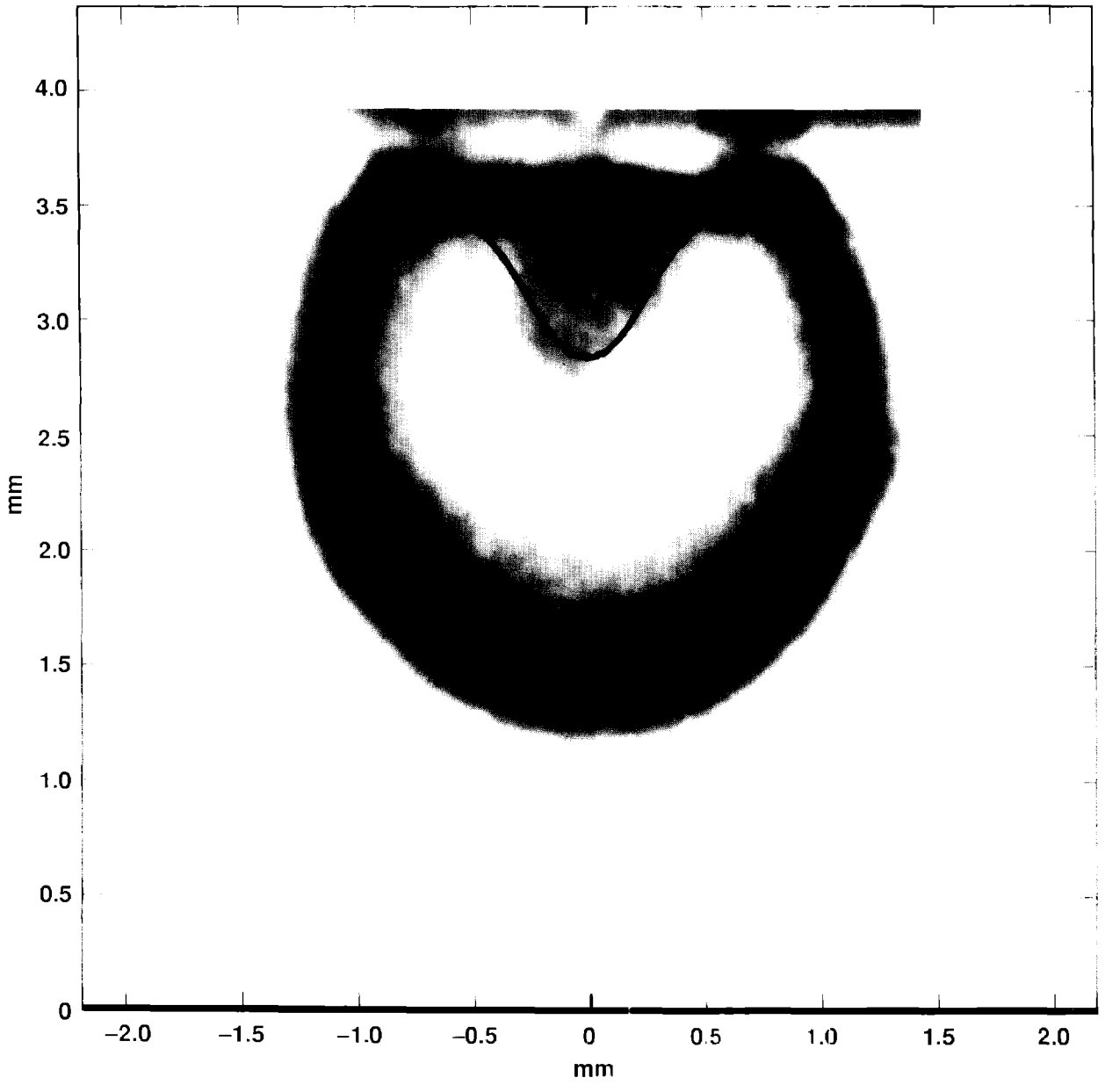

Fig. 16 Comparison of the experimental and calculated bubble shape at 605 μs

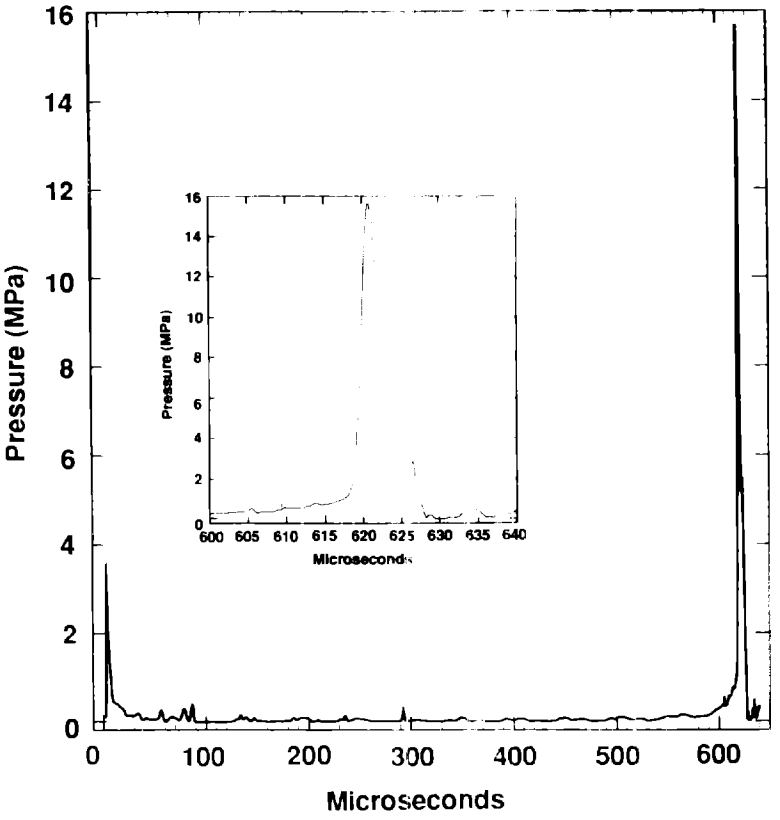

Fig. 17 Calculated pressure at the wall vs. time

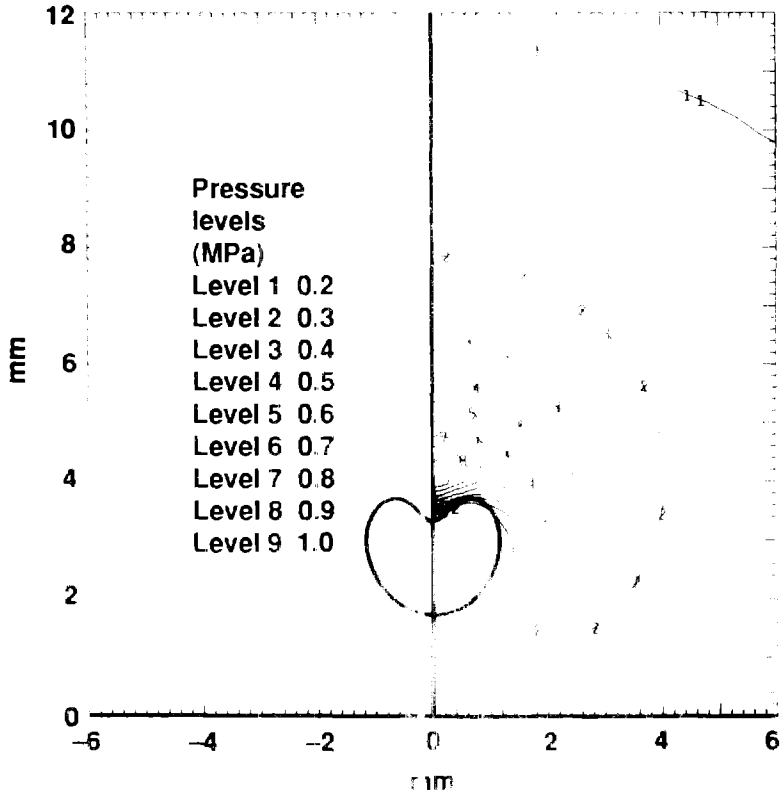

Fig. 18 Isobaric contours at 600 μs